



Studies of high-energy density states using isochoric heating of matter by intense heavy ion beams: the HEDgeHOB Collaboration

To cite this article: N A Tahir *et al* 2008 *Phys. Scr.* **2008** 014023

View the [article online](#) for updates and enhancements.

You may also like

- [Time of flight measurement in heavy-ion collisions with the HADES RPC TOF wall](#)
G. Kornakov, O. Arnold, E.T. Atomssa et al.
- [Spectral composition of secondary electrons based on the Kiefer-Straaten ion track structure model](#)
Thomas Friedrich, Tabea Pfuhl and Michael Scholz
- [Studies of the Core Conditions of the Earth and Super-Earths Using Intense Ion Beams at FAIR](#)
N. A. Tahir, I. V. Lomonosov, B. Borm et al.

Studies of high-energy density states using isochoric heating of matter by intense heavy ion beams: the HEDgeHOB Collaboration

N A Tahir¹, P Spiller¹, A R Piriz², A Shutov³, I V Lomonosov³,
M Schollmeier⁴, A Pelka⁴, D H H Hoffmann⁴ and C Deutsch⁵

¹ Gesellschaft für Schwerionenforschung, Planckstrasse 1, 64291 Darmstadt, Germany

² ETSI Industriales, Universidad de Castilla-La Mancha, 13071 Ciudad Real, Spain

³ Institute for Problems in Chemical Physics, Chernogolovka, Russia

⁴ TU Darmstadt, 64289 Darmstadt, Germany

⁵ LPGP, Université Paris-Sud, 91405 Orsay, France

E-mail: n.tahir@gsi.de

Received 30 October 2007

Accepted for publication 20 March 2008

Published 17 December 2008

Online at stacks.iop.org/PhysScr/T132/014023

Abstract

During the past decade, substantial progress has been made in the technology of highly focused, strongly bunched intense beams of energetic ions. These developments have led to a new concept of studying high energy density (HED) states in matter by isochoric and uniform heating of samples of matter by these intense particle beams. Existing accelerator facilities and those planned for the future, make the Gesellschaft für Schwerionenforschung (GSI), Darmstadt, a unique laboratory worldwide to carry out novel studies in this important field of research. Over the past few years, extensive theoretical work has been carried out to design novel experiments to study the thermophysical properties of HED matter. An overview of this work is presented in this paper highlighting the salient features of this new approach.

PACS numbers: 51.50.+v, 51.60.+a, 51.70+f

(Some figures in this article are in colour only in the electronic version.)

1. Introduction

Intense particle beams uniformly heat extended targets, thereby generating large samples of high energy density (HED) matter with fairly uniform physical conditions [1–5]. It has been proposed that this intrinsic property of energetic ion beams (volume heating of matter), can be exploited to study HED states in the laboratory. Based on detailed theoretical investigations that include sophisticated two- and three-dimensional (2D and 3D) numerical simulations as well as analytic modeling, several interesting experiment designs have been proposed over the past few years [6–28]. One of the proposed schemes named HIHEX (Heavy Ion Heating and EXpansion), considers quasi-isochoric and uniform heating of matter by the ion beam that directly induces exotic

states of high entropy and high pressure in matter, without generating a shock wave. The heated material is then allowed to expand leading to interesting physical states of HED matter including that of an expanded hot liquid, two-phase liquid–gas state, critical parameters or a strongly coupled plasma state. This experimental scheme can be used to study the equation-of-state (EOS) properties of HED matter at subsolid densities. Traditional methods, on the other hand, employ shock compression to carry out such studies. Different drivers including gas guns [29, 30], chemical explosives [31–33] and high power lasers [34–37] have been used to generate the shocks. In some cases even nuclear explosions [38] have been employed for this purpose.

A second experimental setup for HED studies that has been proposed for a heavy ion driver is named LAPLAS

(**L**aboratory **P**lanetary **S**ciences). This latter scheme involves low-entropy compression of a sample material such as hydrogen that is imploded in a multi-layered cylindrical target employing a multiple shock reflection scheme. It has been predicted that such an experiment could generate physical conditions in matter that are expected to exist in the interiors of the giant planets.

Due to its unique accelerator facilities and planned extensive future developments, namely, construction of a new international Facility for Antiprotons and Ion Research (FAIR) [39], the Gesellschaft für Schwerionenforschung (GSI), Darmstadt is a unique laboratory worldwide where these experiments can be performed. The theoretical work that we carried out over the past few years has resulted in an extensive proposal named HEDgeHOB (**H**igh **E**nergy **D**ensity **M**atter **G**enerated by **H**heavy **I**on **B**eams), that outlines the experimental work that will be carried out at the FAIR with HIHEX and LAPLAS as the two main experimental schemes. In this paper, we present an overview of this theoretical work.

In section 2, we describe the FAIR facility, while in section 3, we discuss the problem of isochoric heating and the HIHEX experimental scheme. The importance of the EOS of hydrogen under extreme conditions and the LAPLAS experimental setup together with numerical simulations are presented in section 4. In section 5 are discussed some typical diagnostic techniques for these future experiments while conclusions drawn from this work are noted in section 6.

2. FAIR

The existing heavy ion synchrotron SIS12/18 (12/18 indicates operation modes with different maximum magnetic rigidity) will be used in two different operation modes within the FAIR project. In FAIR stage 1, SIS12/18 will serve as high-energy accelerator, providing for example U^{73+} ions at energies of up to 1000 MeV u^{-1} for the radioactive beam program involving the Super-Fragment Separator (Super-FRS) [40–44] and the connected storage rings CR and NESR. In FAIR stages 2 and 3, SIS12/18 will be used in a fast operation mode with a reduced maximum rigidity of 12 Tm as booster for the new synchrotrons SIS100 and SIS300.

SIS18 operation as driver for the radioactive beam program requires operation with one cycle per second (1 Hz) in the SIS18 mode (18 Tm) and high intensity operation with heavy ion beams, especially acceleration of $2 \times 10^{10} U^{73+}$ ions per machine cycle.

SIS12 operation as booster synchrotron for SIS100, on the other hand, requires operation with four cycles per second (4 Hz) in the SIS12 mode (12 Tm) and high intensity operation with heavy ion beams, especially acceleration of $2.0 \times 10^{11} U^{28+}$ ions per machine cycle and 5.0×10^{12} protons per machine cycle. Pulse-to-pulse mode for operation with all different ion species is also required.

To achieve these beam intensities in SIS12/18, well-specified, high intensity and high quality beams have to be provided by the UNILAC and in stages 2 and 3 by the new dedicated proton injector linac.

In the booster mode, SIS12 will be operated with a dipole ramp rate of 10 T s^{-1} up to a maximum dipole field of 1.2 T,

which corresponds to a maximum magnetic rigidity of 12 Tm. Thereby an average cycle time of 250 ms can be realized and the necessary time for injection of four SIS12 batches into the high-energy synchrotron SIS100 is reduced to about 0.75 s. With RF acceleration at harmonic number $h = 2$ in SIS12, two bunches of ions will be prepared and transferred with each booster cycle to SIS100. Eight of 11 buckets will be filled with four booster cycles.

SIS100 is the main accelerator in the FAIR project. It is a new large synchrotron designed for the magnetic rigidity of 100 Tm, i.e. comparable in size to the large proton synchrotrons PS (CERN) and AGS (BNL). SIS100 is designed for the acceleration of high-intensity and high-energy proton and ion beams. The proposed research program defines the following key parameters:

1. for the radioactive beam program, about 10^{12} uranium ions per second at energies from 400 to 2700 MeV u^{-1} in a single short bunch with pulse lengths from 50 to 100 ns;
2. for the antiproton facility, 6×10^{13} protons per pulse at 29 GeV every 5 s;
3. for plasma physics research, at least 10^{12} uranium ions in a single short bunch (50–100 ns) at energies from 400 to 2700 MeV u^{-1} ; and
4. for the research program with high-energy heavy ion beams, for example, 2×10^9 uranium ions per second at 34 GeV u^{-1} , as booster for the high-energy synchrotron SIS300.

For the acceleration of high intensity uranium beams, U^{28+} ions will be used, since the space charge limit for synchrotron acceleration scales with the factor A/q^2 , i.e. the maximum beam intensity per synchrotron pulse is increased by a factor 6.8 for the charge state 28 compared to 73, which is the average charge state at SIS18 injection energy. In addition, a short synchrotron cycle time of $T = 1 \text{ s}$ is required to achieve the average beam intensity of about 10^{12} uranium ions per second.

Therefore, new technical features are required for SIS100: (i) operation at a very low base pressure of $P = 10^{-12} \text{ mbar}$, i.e. in the XHV range, (ii) careful control of beam losses, especially beam losses due to charge exchange $q = 28\text{--}29$ with residual gas molecules, by implementation of a well-designed collimator systems, (iii) s.c. synchrotron magnet operation at a high ramp rate of 4 T s^{-1} , and (iv) bunch compression for high intensity proton and uranium ion beams to provide a single short bunch with a pulse length of about 50 ns for the production and storage of secondary beams, and installation of two synchrotrons, i.e. SIS100 and SIS300, in one common tunnel.

These technical features define new challenges for the synchrotron design which extend far beyond the conventional design of existing proton synchrotrons.

These planned future developments are schematically shown in figure 1.

3. Isochoric heating of matter by intense ion beam: the HIHEX scheme

If the duration of the ion bunch is shorter than the hydrodynamic response time of the material, the ion energy

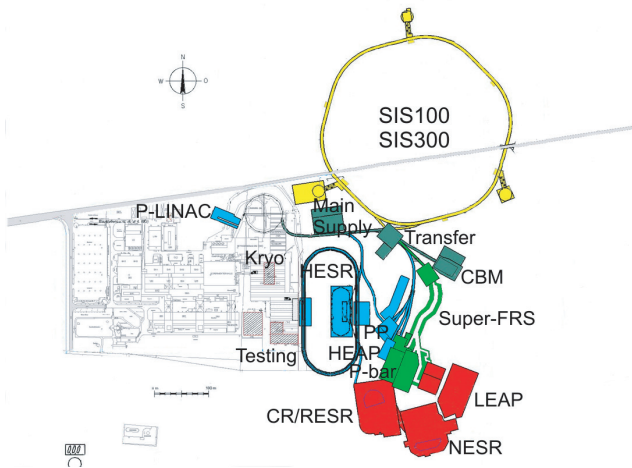


Figure 1. Layout of the future FAIR accelerator facility: Super-FRS (Super Conducting Fragment Separator), HESR (High Energy Storage Ring), HEAP (High Energy Atomic Physics), LEAP (Low Energy Atomic Physics), NESR (New Experimental Storage Ring), CR/RESR (Cooler Ring/Recycled Experimental Storage Ring), PP (Plasma Physics), P-bar (Antiprotons).

will be deposited isochorically. It is also worth noting that recent developments in the field of high intensity petawatt lasers has lead to generation of intense, collimated ultrashort-pulse proton beams [45]. It has been shown [46] that these beams can be used for isochoric heating of matter in a manner similar to the proposed HIHEX technique using heavy ion beams generated by a traditional accelerator. However, there are a number of advantages of using heavy ion beams compared to the laser generated proton beams, as briefly discussed below.

One of the key requirements in studying the EOS of HED matter using isochoric heating by the particle beam, is uniformity of physical conditions in the sample material. Moreover, the size of the sample should be large enough to facilitate the diagnostics. The transverse particle intensity distribution in the case of accelerator delivered heavy ion beams as well as the laser generated proton beams is approximately Gaussian. In order to achieve uniform energy deposition in the target in transverse direction, the target (a cylinder) diameter should be less than the full width at half maximum (FWHM) of the Gaussian intensity distribution. In the case of the heavy ions, for example with the SIS100 beam, one can have a spot size with a FWHM of 2–3 mm that will lead to a specific energy deposition of about 200–300 kJ g⁻¹ in solid lead or gold and one can use a cylindrical target with a radius of 500 μ m. A typical HIHEX experimental setup is shown in figure 2 in which the sample is enclosed within a cylindrical wall of a strong material such as sapphire or LiF that is transparent to infrared, visible and ultraviolet radiation. There is a gap between the solid target and the wall that restricts the material expansion and at the same time allows for diagnostics.

In the case of currently available laser generated proton beams, one can have a beam FWHM of the order of 50 μ m that leads to a specific energy deposition of about 100 kJ g⁻¹, but this would restrict the target size to a radius of the order of 10 μ m.

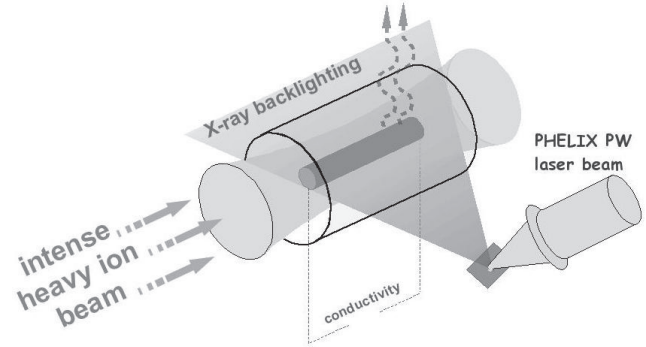


Figure 2. A schematic diagram of cylindrical HIHEX.

In order to achieve uniform energy deposition along the longitudinal direction, the ion range should be large compared to the target length so that the Bragg peak does not lie inside the sample. In the case of accelerator produced heavy ions, one has great flexibility in choosing the particle energy so that one can choose a high energy that will provide a large particle range in the sample material and one may have a target as long as, for example, 1 cm. In the case of laser generated protons, on the other hand, one has little control on the particle energy as it is primarily determined by the laser intensity and energy, which restricts the sample dimensions. Furthermore, accelerators are capable of generating monoenergetic ions, whereas in the case of laser generated protons, the energy spread is of the order of 100% which may lead to non-uniform energy deposition. Another problem that one may face in using highly collimated proton beams and very thin target is the proper target alignment with respect to the beam.

3.1. EOS of HED matter using HIHEX scheme

Figure 3 shows a phase diagram of lead that has been calculated using a wide-range semi-empirical EOS model [47].

The capabilities of various experimental techniques to access different regions of this phase diagram are clearly indicated. It is seen that most of the available data have been obtained using shock wave techniques. In addition to the principal Hugoniot, there are four porous Hugoniot curves and six release isentropes that access the two-phase liquid–gas region and the critical parameters. Using the exploding wire techniques (IEX), critical parameters of lead have also been accessed. However, the major part of the phase diagram that includes the interesting region of strongly coupled plasmas cannot be studied using the traditional methods.

It is seen that following the quasi-isochoric HIHEX heating curve, one can access the entire phase diagram by allowing adiabatic expansion of the heated material. The limits of SIS18 and SIS100 accelerators are also shown in figure 3. It is further to be noted that the estimated critical temperatures for most of the metals are very high (table 1) and cannot be accessed by traditional methods. Detailed numerical simulations have been carried out to design HIHEX experiments (figure 2) using different materials including Pb, Cu, W, Au, Ta, Ir and others. Samples of solid [11, 14, 15, 18, 19, 27, 28] as well as porous [21] materials have been considered. It has been found that using the SIS100

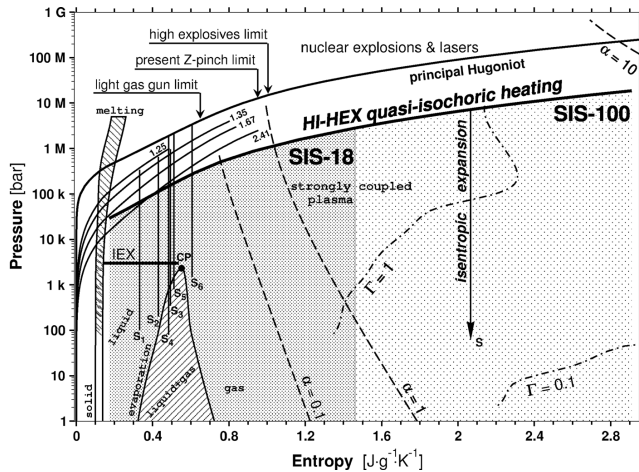


Figure 3. Pressure–entropy phase diagram for lead. All the experimentally studied regions using different techniques are plotted. The principal and porous Hugoniot investigated in shock wave compression experiments (the numbers near Hugoniot curves indicate porosity, $V_{\text{porous}}/V_{\text{solid}}$), the only studied release isentropes (S_1 to S_6) from [31–33, 48] and isobaric expansion (IEX) [49] are shown along with the parameter space which will be accessible with HIHEX technique. Possibilities of shock wave drivers are also plotted using the data from [31–33, 48] for light-gas guns, high explosive generators and for Z-pinch [50]. The physical characteristics such as melting and evaporation curves, the critical point, isolines of ionization degree (α) and non-ideality parameter (Γ) are also shown.

Table 1. Critical point parameters of some metals [51].

	T_c (K)	P_c (kbar)	ρ_c (g cm $^{-3}$)
Lead	5500	2.30	3.10
Gold	8500	6.14	6.10
Zinc	3080	3.30	2.40
Copper	7800	9.00	2.28
Silver	7050	10.64	3.28
Beryllium	8877	2.87	0.40
Iridium	11 640	6.20	3.10
Tin	8175	2.39	1.59
Uranium	9637	7.70	4.50
Aluminum	6250	1.97	0.70
Tungsten	15 750	11.8	4.85
Niobium	19 200	11.10	1.70
Tantalum	13 530	9.93	4.26

beam, one will be able to access the entire phase diagram of all the materials of interest.

Moreover, in HIHEX technique, one is not limited to any specific type of material, but any material can be studied using this method.

It is also to be noted that numerical simulations have shown that the 7 TeV proton beam of the CERN Large Hadron Collider (LHC) can also be used to study HED states in matter [52, 53].

4. Low-entropy compression of hydrogen using intense ion beam: the LAPLAS scheme

Hydrogen is the simplest and most abundant element in the universe. EOS properties of hydrogen under extreme conditions of density and pressure are of great interest to astrophysics and planetary sciences. In addition to that,

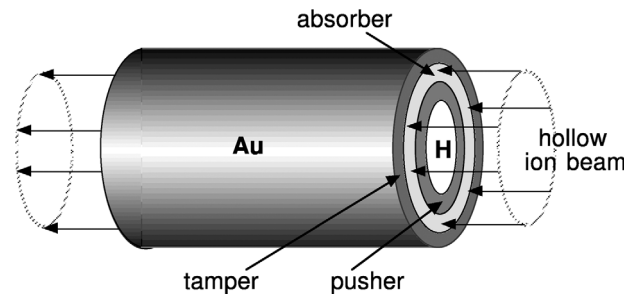


Figure 4. Conceptual setup of LAPLAS scheme.

Wigner and Huntington [54] suggested in 1935 that hydrogen will transform into a metallic state when subjected to ultra high pressures. Later it was predicted that metallic hydrogen may be a room temperature superconductor [55]. Moreover, if stabilized after release of the applied pressure, it could be used as a clean and very efficient fuel for space travel. It has been predicted [56] that metallic hydrogen may be in a metastable state and the sample may remain intact after the applied pressure is removed. Due to the above reasons, this problem has attracted much attention over the past many decades. Both static [57], as well as dynamic [29, 30, 58, 59] configurations have been used to compress hydrogen, but the problem has not yet been solved, although much higher pressures (a few Mbar) have been achieved compared to 0.25 Mbar that was originally suggested [54].

4.1. The LAPLAS scheme

Figure 4 shows the conceptual design of the proposed LAPLAS experiment using an annular focal spot. The target consists of a cylinder of frozen hydrogen that is surrounded by a thick shell of a heavy material, typically gold or lead. One face of the target is irradiated with an intense heavy ion beam that has an annular (ring-shaped) focal spot. We assume that the inner radius of the annulus is larger than the radius of the sample material which is a necessary condition to avoid direct heating of the sample by the ion beam. Moreover, we consider that the outer radius of the focal spot ring is smaller than the outer radius of the surrounding shell. It is seen from figure 4, that a layer of cold material from the outer shell known as ‘pusher’ or ‘payload’, will be created between the sample material and the beam-heated region. The payload plays an important role in placing the compression on the desired adiabat. It is also seen that a cold shell around the beam-heated zone remains as a tamper that confines the implosion for a longer time.

The target length is assumed to be less than the range of the driver ions so that the energy deposition in the longitudinal direction is uniform. The pressure in the beam-heated region increases substantially, launching a shock wave inwards, along the radial direction. The shock wave enters the pusher and is subsequently transmitted into the hydrogen and is reflected at the cylinder axis. The reflected shock wave moves outwards along the radial direction and is re-reflected at the hydrogen–gold boundary. The boundary continues to move inwards, thereby compressing the hydrogen slowly (see figure 5). This scheme generates a low-entropy compression that leads to a very high material density with a relatively

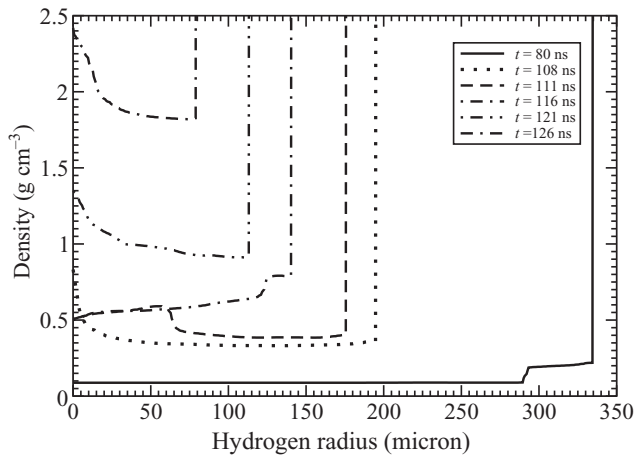


Figure 5. Density versus radius at different times in hydrogen showing the reverberation of the shock between the axis and the hydrogen-gold boundary.

low temperature. Simulations have shown that using the parameters of the SIS100 beam at the FAIR, one would achieve a hydrogen density of $1\text{--}3\text{ g cm}^{-3}$, a pressure of $3\text{--}30\text{ Mbar}$ and a temperature of a few thousand kelvins [6, 8, 10, 11, 15–17, 19–24, 60].

We note that generation of an annular focal spot is a challenging problem. It has been previously demonstrated that a ring-shaped focal spot can be generated using a plasma lens [61]. An alternative approach has recently been suggested to employ an rf-wobbler that will rotate the beam with a very high frequency (of the order of a GHz) that will generate the required focal spot geometry. A detailed analysis of the symmetry issues of energy deposition in the target using such a system have been published elsewhere [62, 63].

4.2. Hydrodynamic stability of the LAPLAS implosion

An issue of possible concern in the LAPLAS experiment may be the hydrodynamic instabilities that could affect the implosion performance, namely Rayleigh–Taylor (RT) and Richtmyer–Meshkov (RM) instabilities. Simple analysis have shown that the LAPLAS target may be stable to these two instabilities [21]. Such an analysis, however, is far from being trivial since in the LAPLAS experiment we have to deal with the extraordinary conditions that arise from the properties of the materials during the implosion. In fact, numerical simulations show that the absorber material is melted and remains in liquid state during most of the implosion time, while the pusher remains in solid state keeping its elastic–plastic properties.

The hydrodynamic instabilities of accelerated solids with elastic–plastic properties is a problem not completely solved yet. There are a couple of theories for the case of the RT instability of a perfectly elastic solid which apply to some particular cases [64, 65]. One of these theories is based on normal modes and applies to the asymptotic regime achieved after the initial transient phase [64]. The other theory is able to describe this initial transient phase but applies only to solid/vacuum interfaces for which the Atwood number is equal to one [66]. Besides, in both cases, implicit solutions are obtained that require numerical calculations and their

extension to more realistic situations that include different initial conditions or the transition from the elastic to the plastic regime may be a very difficult task.

Recently, linear numerical simulations for the case of the RM instability in a perfectly elastic medium have been reported [66].

4.2.1. RT instability in elastic solids. We have developed a new model that allows for the description of the asymptotic regime as well as of the initial transient phase of the RT instability. It applies to different kind of interfaces (solid/solid, solid/fluid) with arbitrary initial conditions and Atwood numbers. Besides, it yields explicit and very precise analytical formulae that agree with the numerical simulations within 15%.

The simplest version of the model can be easily explained in terms of Newton’s second law [17, 67]. Let us consider two semi-infinite incompressible and inviscid fluids that have a surface of contact initially at $y = 0$ and the denser fluid of density ρ_2 lies above the lighter fluid of density $\rho_1 < \rho_2$ in a uniform gravitational field with gravity acceleration g . If the interface between the fluids is initially perfectly planar and equilibrium exists, the fluid elements on each side of the interface immediately above and below it, respectively, must have the same pressure $p_1 = p_2 = p_0$. Now, let us introduce a small perturbation $\xi(x)$ on the interface in such a way that these elements originally at $y = 0$ are quasi-statically translated to the new position $y = \xi(x)$. Since pressure in an incompressible fluid increases linearly with depth, the elements translated to a deeper position ($\xi > 0$) will be at a pressure higher than p_0 (those elements translated to a position $\xi < 0$ will be at a pressure lower than p_0). However, the pressure also increases proportionally to the fluid density so that (for $\xi > 0$) it increases more on the side of the fluid with higher density. Then, pressure of the fluids on each side of the translated interface is $p'_1 = p_0 + \rho_1 g \xi$ and $p'_2 = p_0 + \rho_2 g \xi$, respectively.

Therefore, in the new position, a pressure difference $\Delta p = (\rho_2 - \rho_1)g\xi$ is created across the interface that tends to deform it further. This pressure difference drives the motion of the interface and we can describe this motion by means of Newton’s second law: $m\ddot{\xi} = \Delta p A$, where A is the area of the interface and m is the mass of both fluids involved in the motion. In order to calculate this mass, we must consider that RT instability induces surface modes that decay from the interface exponentially as $\exp(-ky)$, where $k = 2\pi/\lambda$ is the perturbation wave number (λ is the perturbation wavelength). That is, in the linear regime, the intensity of the motion decays with the distance to the interface with a characteristic length k^{-1} . Therefore the total effective mass that participates in the motion is the mass contained within this distance: $m = m_1 + m_2 = \rho_1 A/k + \rho_2 A/k$, where m_1 and m_2 are, respectively, the masses of light and heavy fluids that move when the interface does. From a formal point of view, the exponential decay of the perturbations from the interface with a characteristic scale length equal to k^{-1} follows from the fact that the velocity field for an inviscid fluid is irrotational and incompressible, as can be easily shown from the normal modes analysis. On the other hand, since in the linear regime $k\xi \ll 1$, k^{-1} is the only relevant characteristic scale length that can be involved in the determination of the density profile.

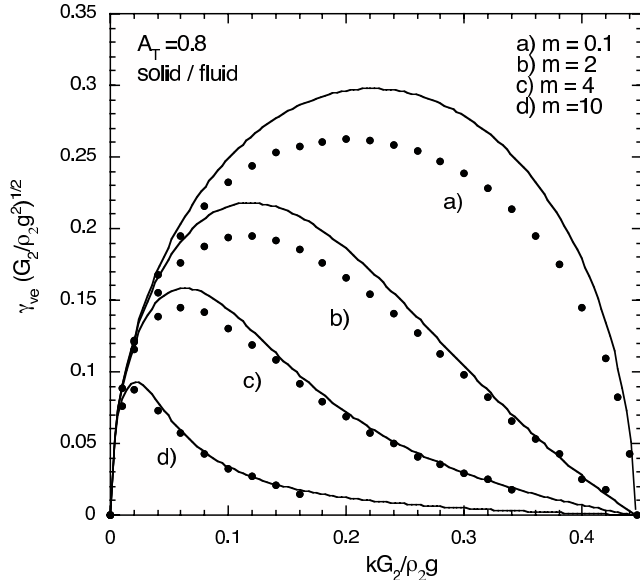


Figure 6. Asymptotic dimensionless growth rate $\gamma_{ve}(G_2/\rho_2 g^2)^{1/2}$ as a function of the dimensionless perturbation wavenumber $kG_2/\rho_2 g$ for a solid/fluid interface, for an Atwood number $A_T = 0.8$ and for several values of the dimensionless viscosity parameter $m = [\mu_1 g(\rho_2/G_2^3)^{1/2}]^{1/2}$. Dots are the exact results of [64] and full lines are given by the present model.

Thus, from the previous equations, the equation of motion of the interface can be written as:

$$\ddot{\xi} = A_T k g \xi, \quad A_T = \frac{\rho_2 - \rho_1}{\rho_2 + \rho_1}, \quad (1)$$

where A_T is the Atwood number. The previous equation is easily integrated to yield the well-known asymptotic exponential growth of the amplitude with time:

$$\xi = \xi_0 \cosh(\gamma t) + \frac{\dot{\xi}_0}{\gamma} \sinh(\gamma t), \quad (2)$$

where $\xi_0 = \xi(t=0)$ and $\dot{\xi}_0 = \dot{\xi}(t=0)$ are, respectively, the initial perturbation amplitude and velocity of the interface, and $\gamma = \sqrt{A_T k g}$ is the asymptotic growth rate. The physical arguments based on elemental hydrostatics used in the derivation of equation (1) clearly show how the driving force $(\rho_2 - \rho_1)g\xi A$ is created across the deformed interface.

Extension of the present arguments to more complex situations involving non-ideal fluids and solids is straightforward. In fact, these effects will cause additional forces F_i on the interface that must be included into the equation of motion. Then, in general we can write:

$$\frac{d}{dt}[(m_1 + m_2)\dot{\xi}] = (\rho_2 - \rho_1)g\xi A + \sum F_i. \quad (3)$$

The only limitation in applying equation (3) is our own skill to correctly calculate or estimate the forces F_i . These forces can be obtained from the constitutive model for the material. For the case of a perfectly elastic solid, we get:

$$F_e^{(n)} \approx -2G_n k(\xi - \xi_0)A, \quad (4)$$

where ξ_0 is the initial value of the perturbation amplitude and $n = 1, 2$ indicates the corresponding medium and G_n is the shear modulus of the material 'n'.

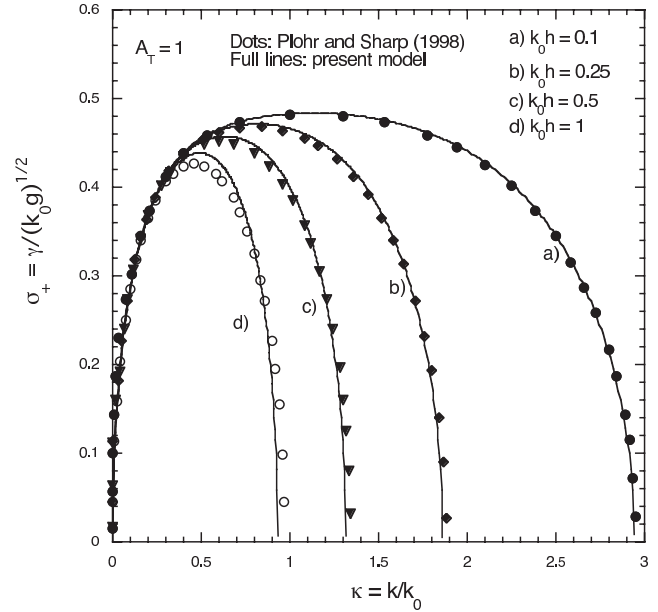


Figure 7. Asymptotic dimensionless growth rate $\sigma_+ = \gamma/(k_0 g)^{1/2}$ as a function of the dimensionless perturbation wavenumber $\kappa = k/k_0$ for $A_T = 1$ and for several values of the parameter $k_0 h$. Dots are the exact results by Plohr and Sharp [65] and full lines are given by the present model.

For the case of a viscous fluid, it turns out:

$$F_v^{(n)} \approx -2\mu_n k \dot{\xi} A, \quad (5)$$

where μ_n is the viscosity of the material 'n'.

Introducing equations (4) and (5) into equation (3), we can obtain the equation of motion of fluid/fluid, solid/solid or solid/fluid interfaces ($n = 2$ for the solid and $n = 1$ for the fluid). For instance, for the case of solid/fluid interfaces, we get:

$$\ddot{\xi} + \frac{\mu_1}{\rho_2}(1 + A_T)k^2 \dot{\xi} = A_T k g \xi - \frac{G_2}{\rho_2}(1 + A_T)k^2(\xi - \xi_0). \quad (6)$$

This equation can be solved analytically to yield an explicit expression for the perturbation amplitude. In figure 6, we show the asymptotic growth rate γ_{ve} for the particular case of Atwood number $A_T = 0.8$ and for several values of the dimensionless viscosity $m = [\mu_1 g(\rho_2/G_2^3)^{1/2}]^{1/2}$. As we can see, the asymptotic growth rate has a cut-off wavenumber $k_c = (\rho_2 - \rho_1)g/(2G_2)$ above which it goes to zero. This cut-off is not affected by the fluid viscosity which, instead, reduces the maximum growth rate. In the figure, dots are given by the exact solution presented in [64] and lines are given by the present model which agree with the exact results within 15%. It is worth noticing that this asymptotic growth rate is achieved after an initial transient phase that lasts a time of the order of γ^{-1} . Thus, for wavenumbers close to the cut-off, the perturbation may grow considerably during the transient phase and, in practice, it may never achieve the asymptotic regime since it may first suffer a transition to the plastic regime. Asymptotic dimensionless growth factor σ_+ as a function of dimensionless perturbation wavenumber is shown in figure 7

We have also studied the effect of the thickness of the solid medium by considering a thin elastic plate (figure 8) [22]. In this case, the interface dynamics is governed

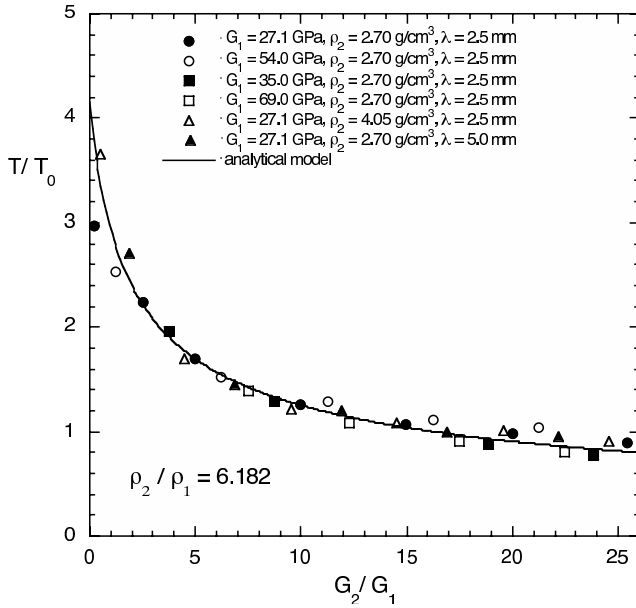


Figure 8. Dimensionless period T/T_0 as a function of the shear moduli ratio G_2/G_1 for $\rho_2/\rho_1 = 6.182$ and different cases.

by the well-known fact that when a normal load is applied on a thin plate, it develops lateral stresses that are much larger than the normal load. In figure 8, we have represented the asymptotic growth rate for different plate thicknesses h and for the particular case of $A_T = 1$ for which the exact solutions of [66] are available for comparison ($k_0 = \rho_2 g / G$). As we can see, thinner plates are more unstable. Dots correspond to the exact solutions and lines are given by the analytical model.

4.2.2. RM instability analysis. A RM-like instability may occur when the shock wave is launched into the pusher from the absorber/pusher interface setting the initial conditions for the RT instability. It may also happen when this shock arrives at the pusher/hydrogen interface. Recently, Plohr and Plohr [66] have shown by means of linear numerical simulations that in the case of elastic media these interfaces must be stable. Using an approach similar to the one presented in the previous subsection for the analysis of the RT instability, we have studied the RM in elastic solids [23]. Assuming that now the characteristic length of decay from the interface of the velocity field is αk^{-1} (α is taken equal to 1.55 in order to best fit the simulations), we find the interface equation of motion for a solid/solid interface (a similar approach yields the equation of motion for solid/fluid interfaces):

$$\ddot{\xi} = \omega^2(\xi - \xi_{0*}), \quad T = \frac{2\pi}{\omega} = 1.55 \sqrt{\frac{1 + \rho_2/\rho_1}{2(1 + G_2/G_1)}}, \quad (7)$$

where $\xi_{0*} = \xi_0(1 - v/u_i)$ is the post-shock initial amplitude before the interface starts to be deformed by the eventual development of the instability (u_i is the incident shock velocity and v is the velocity gained by the interface in the interaction with the shock).

Equation (7) can be easily integrated with the initial conditions $\xi(t=0) = \xi_{0*}$ and $\dot{\xi}(t=0) = v_0$ to yield:

$$\xi = \xi_{0*} + \frac{v_0}{\omega} \sin \omega t, \quad (8)$$

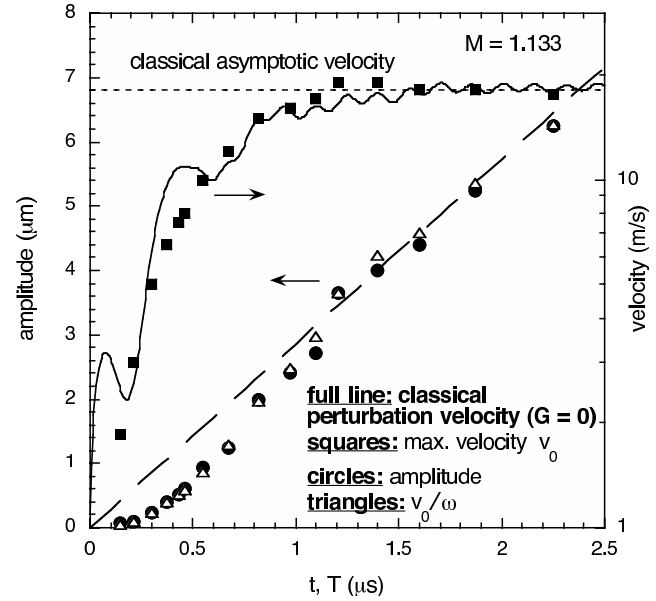


Figure 9. Maximum oscillation velocity v_0 (squares), oscillation amplitude (circles) and the relationship $v_0 T/2\pi$ (triangles) as a function of the oscillation period T . Dashed line is the relationship $v_0^{as} T/2\pi$ as a function of the period T ; full line is the perturbation velocity v_{cl} for the classical case ($G_v = 0$) as a function of time, and dotted line indicates the classical asymptotic velocity.

where $t = 0$ is the instant after the interaction. v_0 is some initial velocity that cannot be calculated from the present analysis and any prescription for it would be equivalent to the prescriptions used in the impulsive model [68]. Actually the calculation of v_0 would require a self-consistent treatment like that presented in [69–71]. Nevertheless, equation (8) is useful as it shows that oscillations must take place around a mean value equal to ξ_{0*} that is lower than the initial perturbation amplitude ξ_0 , in agreement with the results of the numerical simulations [66]. This is a distinctive fact of the RM flow in elastic materials that is not observed in gas dynamics when restoring forces are present as a consequence, for instance, of ablation [72, 73] or surface tension [74]. In those cases oscillations are observed to occur around a mean value equal to zero. Equations (7) and (8) show that in elastic materials the different behavior is caused by the stress free conditions existing at $t = 0$, immediately after the interaction of the incident shock with the interface. Such a condition is preserved during the interaction because of its very short duration.

In figure 9, we have compared the oscillation period given by the model with extensive 2D numerical simulations. In figure 10, we show the maximum oscillation velocity v_0 (squares) and the oscillation amplitude (circles) as a function of the oscillation period T . Triangles represent $v_0 T/2\pi$ showing that the oscillation amplitude is given by this relationship in agreement with equation (8). As we can appreciate, the maximum velocity v_0 achieves an asymptotic value for relatively long periods T and, for these cases, the oscillation amplitude grows linearly with T . In the same figure, we show the instantaneous velocity of the perturbations v_{cl} for the classical case ($G_v = 0$) as a function of time. As we can see, the initial velocity v_0 approximately coincides with the instantaneous velocity of the perturbations at the time

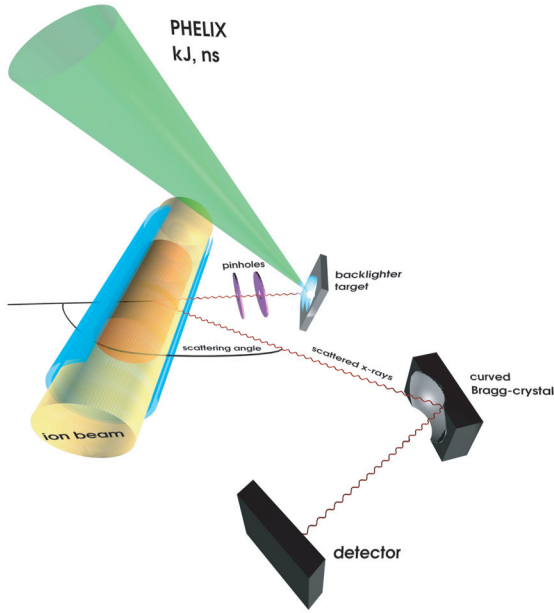


Figure 10. Implementation of the x-ray scattering diagnostics in the HIHEX experiment. The shielding (e. g. Pb or Au plates) that is necessary to prevent parasitic scattering into the detector is not shown.

$t = T$: $v_0 \approx v_{cl}(t = T)$. That is, the initial velocity v_0 to be used in equation (8) is just the instantaneous velocity such as that given by the theory of Wouchuk [70, 71] for the classical case, calculated at a time equal to the oscillation period T . In other words, for times shorter than the characteristic time T the effects of the elastic properties of the material are not felt and the instability starts to grow classically. At a time of the order of the period T the elastic effects are felt and the classical perturbation velocity v_{cl} at $t = T$ is taken as the initial velocity for the later evolution of the instability. As we can see, for relatively short periods, the initial velocity corresponds to the value of the classical velocity during the initial transient phase before the asymptotic regime is reached. Therefore, the calculation of the initial velocity using the Richtmyer prescription would be in error even in those cases for which such a prescription may give a good approximation for the asymptotic growth rate. A similar case may happen in other RM-like flows such as, for instance, the one that develops in ablation fronts [72, 73]. In such a case, the characteristic time associated with the stabilizing ablation process will determine the initial perturbation velocity required to calculate the correct oscillation amplitude.

5. Diagnostics

Efficient diagnostics is the backbone to the success and usefulness of any experiment. Because of the high density and exotic behavior of the electrons in the HED samples, the standard diagnostic techniques will fail. New diagnostic techniques are therefore needed and are being developed for the HIHEX and LAPLAS experiments that will have high spatial and temporal resolution. One such diagnostic methods that involves the high power laser, PHELIX [75], at GSI is discussed in this section.

Recently, an extension of Thomson scattering as a plasma diagnostics [76, 77] for x-rays has been proposed [78] and demonstrated on solid density and super-dense plasmas [79–81]. The scattering of electromagnetic waves by charged particles is therefore a viable tool to diagnose low as well as high density plasmas providing means for simultaneous determination of plasma temperature, density and charge state.

Due to the complexity of theoretical models describing the radiative properties of HED matter, sometimes it is difficult to interpret the experimental data on spectroscopic measurements of temperature, density or the population of various species (like ions, neutrals and molecules). Therefore, an additional independent diagnostic method would considerably advance the understanding of the physical properties of HED matter. For this purpose, spectrally resolved x-ray Thomson scattering (XRTS) [79] driven by the PHELIX has been proposed [82]. This method is supposed to provide valuable information about the free electron density, the electron temperature, the chemical composition and the plasma coupling parameter.

Due to the extremely small Thomson scattering cross section of $6.67 \times 10^{-25} \text{ cm}^2$, a photon number of about 10^{15} [78, 82] at energies of a few keV is needed for diagnostics. In order to provide such high photon numbers, a laser intensity of more than 10^{14} Wcm^{-2} and a total laser energy of a few hundred Joules at the second harmonic is required [83]. A possible scheme of the x-ray scattering diagnostics for the HIHEX experiment is shown in figure 5. This experimental configuration will allow flexibility in the choice of the scattering angle to either probe collective or non-collective properties of the matter.

The PHELIX beam will be used to generate 10^{15} photons [84] with an energy of 4.75 keV of the Ti $\text{He}_{\alpha}(1s^2-1s2p^1P)$ line ($\lambda = 0.26 \text{ nm}$). Assuming that the x-ray source (Ti foil) is placed at a distance of 5 mm from the HED sample, one can estimate the intensity of the probe x-ray beam: if the beam diameter on the sample is 0.3 mm (limited by a pinhole), about 10^{12} photons will probe the target. Following the approach of Chihara [85–88], the scattering cross section depends on the classical Thomson cross section, σ_{Th} , the scattering angle, ϑ , and the dynamic structure factor, $S(\omega, k)$, of all electrons in the HED sample:

$$\sigma \propto \sigma_{Th}(1 + \cos^2 \vartheta)S(\omega, k). \quad (9)$$

This cross section can be estimated as $\sigma \approx 4 \times 10^{-26} \text{ cm}^2 \text{ sr}^{-1}$. The scattering angle determines a collective or non-collective mode of the scattering. In the case of the collective mode, fluctuations on a longer spatial scale than the Debye length are sampled and plasmon features in the scattering spectrum appear [81]. In the non-collective mode, shorter spatial scales are probed and the spectrum reflects the Doppler shifts due to thermal motion of the electrons [79].

The quantity defining whether it is collective or non-collective mode is the scattering parameter α :

$$\alpha := \frac{1}{k\lambda_D} \approx \frac{\lambda_0}{4\pi\lambda_D \sin(\vartheta/2)} \quad (10)$$

with the Debye length λ_D , transferred photon momentum $\hbar k$ and incident wavelength λ_0 [76, 77]. It is clear that in

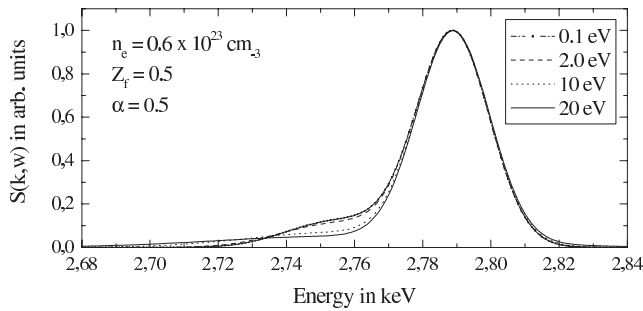


Figure 11. Theoretical x-ray scattering spectrum. The image shows the dynamic structure factors $S(k, \omega)$ convoluted with a Gaussian instrument response of 25 eV FWHM. The probe radiation was assumed to be Cl-He $_{\alpha}$ ($E = 2.789$ keV) that is scattered on an ion beam heated hydrogen sample with $n_e = 0.6 \times 10^{23} \text{ cm}^{-3}$ and various temperatures T_e . The scattering angle is $\theta = 160^\circ$ [91].

the HED regime the usual definition of α in terms of the Debye length breaks down. In order to describe scattering in HED plasmas the generalized scattering parameter $\alpha = (ks)^{-1}$, where s , the characteristic screening length of the electrostatic interactions, is introduced. As the plasma becomes degenerate, the Debye length does not represent anymore the screening of the Coulomb forces. However, the classical results are still valid if, instead of using the kinetic temperature, they are evaluated at the effective temperature $T_{\text{cf}} = (T_e^2 + T_q^2)^{1/2}$ with $T_q = T_F / (1.3251 - 0.1779\sqrt{r_s})$, T_F is the Fermi temperature, r_s is the ratio between the mean particle distance d and Bohr radius r_B [80].

Given the size of the HED sample, at least 10^8 photons sr^{-1} are scattered. Using a spatially resolving imaging crystal spectrometer [89, 90], one can achieve a collection efficiency of about 10^{-4} sr and thus a capture of 10^4 photons per shot.

The detection efficiency of modern CCD x-ray detectors or image plates is sufficient to acquire the spectrum in a single shot. The spectra are expected to differ from the optical spectra: the Compton shift of scattered photons (0–90 eV) will be noticeable (see figure 5) and the spectrum will not be symmetric due to the dynamic structure factors at each side of the central wavelength, related by $S(-\omega, k) \propto \exp(-\hbar\omega/k_B T_e) S(\omega, k)$. This is not important in the optical case ($\hbar\omega \ll k_B T_e$) but for x-rays and collective scatter would yield a single plasmon peak shifted by the plasma frequency as well as Compton shift from the incident wavelength. Figure 11 shows a theoretical scatter spectrum $S(\omega, k)$ for Cl-He $_{\alpha}$ ($E = 2.789$ keV) on dense hydrogen plasma [91]. The image shows the dynamic structure factors $S(k, \omega)$ that were convoluted with a Gaussian instrument response of 25 eV FWHM. The probe radiation is scattered on an ion beam heated hydrogen sample with $n_e = 0.6 \times 10^{23} \text{ cm}^{-3}$ and various temperatures T_e . The scattering angle is $\theta = 160^\circ$ and therefore the scattering parameter α ranges between 0.26 and 0.5. Thus the scattering is inelastic and the width of the red-shifted free electron component directly shows the temperature of the sample.

6. Conclusions

This paper presents an overview of the theoretical work that has been carried out to assess the potential of intense

beams of energetic heavy ions to study HED states in matter. The work has been done in connection with the heavy ion accelerator facilities that will be constructed at the FAIR at Darmstadt. It has been shown that one may employ an intense ion beam using two very different configurations to do such studies. One scheme is named HIHEX that involves isochoric and uniform heating of matter by the beam which is followed by subsequent isentropic expansion of the heated material. Numerical simulations have shown that using the parameters of the beam at FAIR, one will be able to access all the interesting physical states of HED matter (expanded hot liquid, two-phase liquid–gas state, critical parameters and strongly coupled plasmas) of any material of interest.

The second proposal considers low-entropy compression of a sample material such as hydrogen that is imploded in a multi-layered cylindrical target driven by an ion beam with an annular focal spot. Numerical simulations of this scheme have shown that one can generate physical conditions in hydrogen that are expected to exist in the interiors of the giant planets. This scheme is named LAPLAS. The problem of generation of a beam with an annular focal spot and the hydrodynamic stability of the LAPLAS implosion has also been discussed. Finally, a new diagnostic method that uses Thomson scattering to measure density, temperature and chemical composition of very high density plasmas has also been described.

References

- [1] Tahir N A et al 1998 *Phys. Plasmas* **5** 4426
- [2] Tahir N A et al 1999 *Phys. Rev. E* **60** 4715
- [3] Tahir N A et al 2000 *Phys. Rev. E* **61** 1975
- [4] Tahir N A et al 2000 *Phys. Rev. E* **62** 1224
- [5] Tahir N A et al 2001 *Phys. Rev. E* **63** 036407
- [6] Tahir N A et al 2001 *Phys. Rev. E* **63** 016402
- [7] Tahir N A et al 2002 *Laser Part. Beams* **20** 393
- [8] Piriz A R et al 2002 *Phys. Rev. E* **66** 056403
- [9] Hoffmann D H H et al 2002 *Phys. Plasmas* **9** 3651
- [10] Tahir N A et al 2003 *Phys. Rev. B* **67** 184101
- [11] Tahir N A et al 2003 *Phys. Rev. Spec. Top. Accel. Beams* **6** 020101
- [12] Temporal M et al 2003 *Laser Part. Beams* **21** 609
- [13] Tahir N A et al 2004 *Laser Part. Beams* **22** 485
- [14] Tahir N A et al 2005 *Phys. Rev. Lett.* **95** 035001
- [15] Tahir N A et al 2005 *Nucl. Instrum. Methods A* **544** 16
- [16] Piriz A R et al 2005 *Nucl. Instrum. Methods A* **544** 27
- [17] Piriz A R et al 2005 *Phys. Rev. E* **72** 056313
- [18] Tahir N A et al 2006 *Nucl. Instrum. Methods B* **245** 85
- [19] Tahir N A et al 2006 *J. Phys. IV France* **133** 1059
- [20] Tahir N A et al 2006 *J. Phys. A: Math. Gen.* **39** 4755
- [21] Tahir N A et al 2006 *J. Phys. High Energy Density* **2** 21
- [22] Piriz A R et al 2006 *Laser Part. Beams* **24** 275
- [23] Piriz A R et al 2006 *Phys. Rev. E* **74** 037301
- [24] López Cela et al 2006 *Laser Part. Beams* **24** 427
- [25] Piriz A R et al 2007 *Nucl. Instrum. Methods A* **577** 250
- [26] Piriz A R et al 2007 *Contrib. Plasma Phys.* **47** 213
- [27] Tahir N A et al 2007 *Nucl. Instrum. Methods A* **577** 238
- [28] Tahir N A et al 2007 *Contrib. Plasma Phys.* **47** 223
- [29] Nellis W J et al 1992 *Phys. Rev. Lett.* **68** 2937
- [30] Weier S T et al 1996 *Phys. Rev. Lett.* **76** 1860
- [31] van Thiel M (ed) 1977 Compendium of shock wave data Lawrence Livermore Laboratory Report UCRL-50108
- [32] Marsh S P (ed) 1980 *LASL Shock Hugoniot Data* (Berkeley, CA: University of California Press)

- [33] Zhernokletov M V *et al* 1996 *Experimental Data on Shock Compression and Adiabatic Expansion of Condensed Materials at High Energy Density* (Chernogolovka: IPCP RAS) (in Russian)
- [34] Löwer Th *et al* 1993 *Phys. Rev. Lett.* **72** 3186
- [35] Cauble R *et al* 1993 *Phys. Rev. Lett.* **70** 2102
- [36] Koenig M *et al* 1995 *Phys. Rev. Lett.* **74** 2260
- [37] Batani D *et al* 2000 *Phys. Rev. B* **61** 9287
- [38] Vladimirov A S *et al* 1984 *Sov. Phys.—JETP Lett.* **39** 85
- [39] Henning W F 2004 *Nucl. Instrum. Methods B* **214** 211
- [40] Tahir N A *et al* 2003 *Nucl. Instrum. Methods B* **204** 282
- [41] Geissel H *et al* 2003 *Nucl. Instrum. Methods B* **204** 71
- [42] Tahir N A *et al* 2005 *J. Phys. D: Appl. Phys.* **38** 1828
- [43] Tahir N A *et al* 2007 *Laser Part. Beams* **25** 295
- [44] Tahir N A *et al* 2008 *Laser Part. Beams* **26** 273
- [45] Snavely R A *et al* 2000 *Phys. Rev. Lett.* **85** 2945
- [46] Patel P K *et al* 2003 *Phys. Rev. Lett.* **91** 125004
- [47] Lomonosov I V 2007 *Laser Part. Beams* **25** 567
- [48] McQueen R G 1970 *High Velocity Impact Phenomena* ed R Kinslow (New York: Academic) p 293
- [49] Gathers G R 1986 *Rep. Prog. Phys.* **49** 341
- [50] Knudson M D *et al* 2001 *Phys. Rev. Lett.* **87** 225501
- [51] Lomonosov I V 2003 Private communication
- [52] Tahir N A *et al* 2005 *Phys. Rev. Lett.* **94** 135004
- [53] Tahir N A *et al* 2005 *J. Appl. Phys.* **97** 083532
- [54] Wigner E and Huntigton H B 1935 *J. Chem. Phys.* **3** 764
- [55] Ashcroft N W *et al* 1968 *Phys. Rev. Lett.* **21** 1748
- [56] Brovman E G *et al* 1972 *Sov. Phys.—JETP* **34** 1300
- [57] Mao H K and Hemley R J 1994 *Rev. Mod. Phys.* **66** 671
- [58] Ternovoi V Ya *et al* 1999 *Physica B* **265** 6
- [59] Celliers P M *et al* 2000 *Phys. Rev. Lett.* **84** 5564
- [60] López Cela J J *et al* 2005 *J. Phys.: Appl. Phys.* **29** 247
- [61] Neuner U *et al* 2000 *Phys. Rev. Lett.* **85** 4518
- [62] Piriz A R *et al* 2003 *Phys. Rev. E* **67** 017501
- [63] Piriz A R *et al* 2003 *Plasma Phys. Control. Fusion* **E 45** 1733
- [64] Terrones G *et al* 2005 *Phys. Rev. E* **71** 036305
- [65] Plohr J N and Sharp D H 1998 *Z. Angew. Math. Phys.* **49** 786
- [66] Plohr J N and Plohr B J 2005 *J. Fluid Mech.* **E 537** 55
- [67] Piriz A R *et al* 2006 *Am. J. Phys.* **74** 1095
- [68] Richtmyer R D 1996 *Commun. Pure Appl. Math.* **13** 297
- [69] Velikovich A L 1996 *Phys. Fluids* **8** 1666
- [70] Wouchuk J G and Nishihara K 1997 *Phys. Plasmas* **4** 1028
- [71] Wouchuk J G 1997 *Phys. Rev. E* **63** 056303
- [72] Goncharov V N 1999 *Phys. Rev. Lett.* **E 82** 2091
- [73] Goncharov V N *et al* 2006 *Phys. Plasmas* **E 13** 012702
- [74] Mikaelian K O *et al* 1990 *Phys. Rev. A* **42** 7211
- [75] Neumayer P *et al* 2005 *Laser Part. Beams* **23** 385
- [76] Kunze H J 1968 *Plasma Diagnostics* (Amsterdam: North-Holland)
- [77] Sheffield J 1975 *Plasma Scattering of Electromagnetic Radiation* (New York: Academic)
- [78] Landen O L *et al* 2001 *J. Quantum. Spectrosc. Radiat. Transfer* **71** 465
- [79] Glenzer S H *et al* 2003 *Phys. Plasmas* **10** 2433
- [80] Gregori G *et al* 2004 *Phys. Plasmas* **11** 2754
- [81] Glenzer S H *et al* 2007 *Phys. Rev. Lett.* **98** 065002
- [82] Riley D and Rosmej F B 2004 *GSI Report* p 61
<http://www-aix.gsi.de/plasma2003>
- [83] Neumayer P *et al* 2006 *Sci. Instrum.* **77** 10F317
- [84] Urry M K *et al* 2006 *J. Quantum. Spectrosc. Radiat. Transfer* **99** 636
- [85] Chihara J 1987 *J. Phys. F: Met. Phys.* **17** 295
- [86] Chihara J 2000 *J. Phys.: Condens. Matter* **12** 231
- [87] Gregori G *et al* 2003 *Phys. Rev. E* **67** 5971
- [88] Höll A *et al* 2004 *Eur. Phys. J. D* **29** 159
- [89] Faenov A Ya *et al* 1994 *Physica Scripta* **50** 333
- [90] Rosmej *et al* 2002 *Nucl. Instrum. Methods A* **495** 29
- [91] Schollmeier M *et al* 2006 *Laser Part. Beams* **24** 335